## COMMUNICATION

Check for updates

# Ultrathin Ti-doped WO₃ nanosheets realizing selective photoreduction of CO₂ to CH₃OH†

Peiquan Ling,‡[a] Juncheng Zhu,‡[a] Zhiqiang Wang,[a] Jun Hu,[a] Junfa Zhu, [ID] [a]
Wensheng Yan, [ID] [a] Yongfu Sun [ID] *[a,b] and Yi Xie [ID] *[a,b]

Arduous CO₂ activation and sluggish charge transfer retard the photoreduction of CO₂ to CH₃OH with high efficiency and selectivity. Here, we fabricate ultrathin Ti-doped WO₃ nanosheets possessing approving active sites and optimized carrier dynamics as a promising catalyst. Quasi *in situ* X-ray photoelectron spectroscopy and synchrotron–radiation X-ray absorption near-edge spectroscopy firmly confirm that the true active sites for CO₂ reduction are the W sites rather the Ti sites, while the Ti dopants can facilitate charge transfer, which accelerates the generation of crucial COOH* intermediates as revealed by *in situ* Fourier-transform infrared spectroscopy and density functional theory calculations. Besides, the Gibbs free energy calculations also validate that Ti doping can lower the energy barrier of CO₂ activation and CH₃OH desorption by 0.22 eV and 0.42 eV, respectively, thus promoting the formation of CH₃OH. In consequence, the Ti-doped WO₃ ultrathin nanosheets show a superior CH₃OH selectivity of 88.9% and reach a CH₃OH evolution rate of 16.8 μmol g⁻¹ h⁻¹, about 3.3 times higher than that on WO₃ nanosheets. This work sheds light on promoting CO₂ photoreduction to CH₃OH by rational elemental doping.

Artificial photosynthesis, which involves the conversion of carbon dioxide (CO₂) into value-added fuels by solar energy, provides a sustainable way to solve the disturbing energy crisis and climate change.[1–4] Various carbon-containing products can be acquired through the CO₂ photoreduction reaction, among which methanol (CH₃OH) is one of the liquid products with the most potential due to its extensive applications.[5–7] For instance, CH₃OH can be directly used in fuel cells[8] and is

*[a]Hefei National Research Center for Physical Sciences at the Microscale, National Synchrotron Radiation Laboratory, University of Science and Technology of China, Hefei 230026, China. E-mail: yfsun@ustc.edu.cn, yxie@ustc.edu.cn*
*[b]Institute of Energy, Hefei Comprehensive National Science Center, Hefei 230031, China*
†Electronic supplementary information (ESI) available. See DOI: https://doi.org/10.1039/d2nr02364d
‡ These authors contributed equally to this work.

the precursor of numerous fundamental chemicals like aromatics, C₂H₄, methyl methacrylate and fatty acid methyl esters.[5,9] It is reported that the global demand for CH₃OH can reach more than 100 million tons per year.[10] Unfortunately, the product selectivity towards CH₃OH in the conversion of CO₂ with H₂O is still insufficient and unsatisfactory. Obstacles arise from the arduous activation of inert CO₂ molecules (C=O dissociation energy of ∼750 kJ·mol⁻¹).[11,12] Most importantly, the 6-electron transfer process during CH₃OH formation causes strict kinetic limitation, making it harder to generate CH₃OH than other products (*e.g.* CO).[13–15] In addition, many existing photocatalysts suffer from a narrow light adsorption range and the poor separation efficiency of photogenerated carriers, which hinder the charge transfer from the catalysts to the adsorbed CO₂.[16–20] Hence, designing catalysts with outstanding carrier dynamics and approving active sites is essential for realizing highly efficient CO₂ photoreduction into CH₃OH.

To meet the above requirements, constructing ultrathin two-dimensional (2D) nanosheets with appropriate elemental doping is a very promising solution. On the one hand, ultrathin 2D nanosheets can provide abundant active sites for CO₂ adsorption and activation due to their high specific surface area and sufficient uncoordinated atoms.[21–23] Their light absorption ability is also different from that of the traditional bulk catalysts, while the efficiencies of photogenerated carrier separation and charge transfer can be promoted thanks to their reduced migration paths.[24–28] On the other hand, elemental doping can regulate the electron structure of active atoms, further expediting CO₂ activation and reduction.[29,30] It can also change the band structure of catalysts and extend their light absorption range, making the catalysts more suitable for CO₂ photoreduction.[31–33] Furthermore, suitable elemental doping can optimize the photogenerated carrier dynamics, alter the reaction energy barrier and control reaction intermediates, enhancing product selectivity towards the desired species.[29,30,34] Therefore, it is prospective to boost CO₂ photoreduction to CH₃OH through synthesizing ultrathin 2D

nanosheets with elemental doping. In this regard, inexpensive and eco-friendly tungsten oxide ($WO_3$) is one of the promising candidates, thanks to its suitable band gap, good light-harvesting ability and easily tunable electron structure.[35,36] Although $WO_3$ nanosheets have been applied in many photochemical fields,[36–38] their performance in $CO_2$ photoreduction to $CH_3OH$ still lacks exploration.

In this work, Ti-doped $WO_3$ ultrathin nanosheets were fabricated *via* an acid-assisted method. X-ray photoelectron spectroscopy (XPS), synchrotron–radiation X-ray absorption near-edge spectroscopy (XANES) and element mappings show the successful doping of Ti into $WO_3$ nanosheets, while photoluminescence (PL) and time-resolved photoluminescence spectra (TRPL) reveal the enhanced separation of photogenerated carriers due to the Ti doping. Besides, quasi *in situ* XPS spectra and quasi *in situ* XANES spectra firmly validate that the true active sites are the W sites rather the Ti sites, where the Ti dopants facilitate the charge transfer, which is beneficial for the formation of COOH* species, one of the most important intermediates for carbon products during $CO_2$ reduction. *In situ* Fourier-transform infrared (FTIR) spectroscopy demonstrates this conclusion by the stronger intensity of COOH* species on Ti-doped $WO_3$ nanosheets. In addition, density functional theory (DFT) calculations confirm that Ti doping can strengthen the bonding between COOH* intermediates and catalysts, while the energy barrier of $CO_2$ activation and $CH_3OH$ desorption is decreased by 0.22 eV and 0.42 eV, respectively, which dramatically facilitates the formation of $CH_3OH$. As a result, the Ti-doped $WO_3$ ultrathin nanosheets show a superior $CH_3OH$ selectivity of 88.9% and achieve a $CH_3OH$ evolution rate of 16.8 μmol $g^{-1}$ $h^{-1}$, about 3.3 times higher than that on the $WO_3$ nanosheets. This work offers an effective approach to enhance the conversion of $CO_2$ and $H_2O$ into $CH_3OH$ through elemental doping.

To obtain a non-toxic and efficient catalyst for $CO_2$ photoreduction, the ultrathin Ti-doped $WO_3$ nanosheets (called Ti–$WO_3$ nanosheets for short) were fabricated *via* an acid-assisted method. The powder X-ray diffraction (XRD) patterns of the Ti–$WO_3$ nanosheets could be indexed well to JCPDS no. 89-1287 and no additional peak was detected, indicating the successful synthesis of pure tetragonal $WO_3$ (Fig. 1A). The transmission electron microscopy (TEM) image showed that Ti-doped $WO_3$ had a sheet-like morphology (Fig. 1B). Meanwhile, the high-resolution TEM (HRTEM) image showed two interplanar spacings of 0.367 nm and 0.382 nm with a dihedral angle of 90°, corresponding to the (200) and (001) planes of tetragonal $WO_3$, which demonstrated their [010] orientation (Fig. 1C). The atomic force microscopy (AFM) image demonstrated that the thickness of the Ti–$WO_3$ nanosheets was about 2.20 nm (Fig. 1D), which was approximately the thickness of the triple-unit-cell slab along the [010] direction, illustrating the successful fabrication of ultrathin Ti–$WO_3$ nanosheets. For comparison, the undoped $WO_3$ nanosheets (called $WO_3$ nanosheets for short) were obtained without the addition of Ti sources during the synthesis. The $WO_3$ nanosheets had the same crystalline phase, growth orientation and thickness as the Ti–$WO_3$ nanosheets (Fig. S1†). It is worth mentioning that
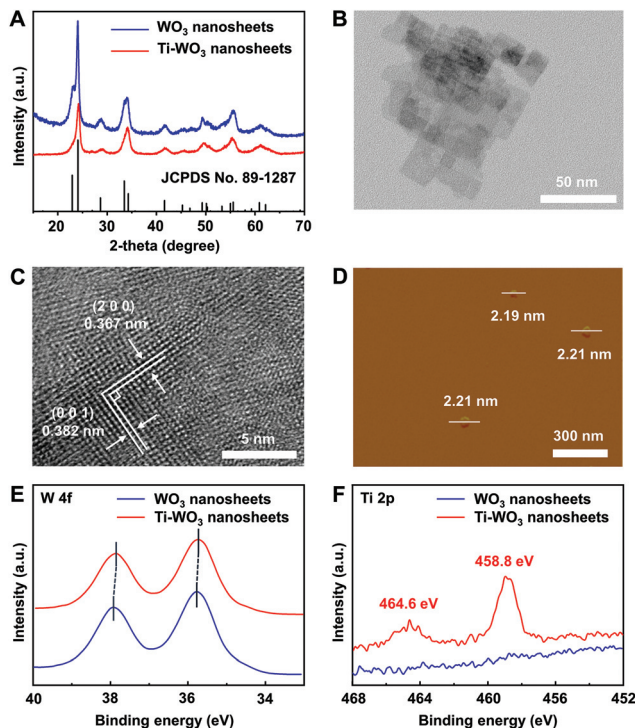


**Fig. 1** (A) XRD patterns of the Ti–$WO_3$ nanosheets and the $WO_3$ nanosheets. (B) TEM image of the Ti–$WO_3$ nanosheets. (C) HRTEM image of the Ti–$WO_3$ nanosheets, showing the 0.367 nm and 0.382 nm interplanar distances that matched well with the $d_{200}$ and $d_{001}$ planes, respectively. (D) AFM image of the Ti–$WO_3$ nanosheets. (E) XPS spectra of W 4f and (F) Ti 2p for the Ti–$WO_3$ nanosheets and the $WO_3$ nanosheets.
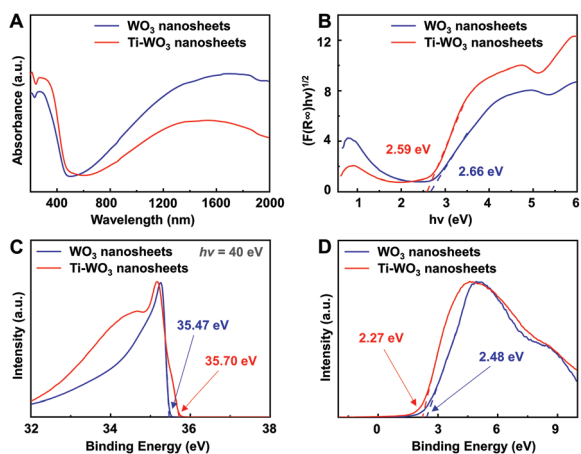
the crystallinity of the Ti–$WO_3$ nanosheets was lower than that of the $WO_3$ nanosheets (Fig. 1A), which could be ascribed to the successful Ti doping into $WO_3$.[39,40] In addition, the Ti doping also slightly decreased the interplanar spacings in the Ti–$WO_3$ nanosheets (Fig. 1C and S1†), which was in agreement with a previous study.[40]

To further confirm that the Ti dopants had been doped in $WO_3$ nanosheets, X-ray photoelectron spectroscopy (XPS) of W 4f and Ti 2p was performed. As shown in Fig. 1E, there were two peaks at around 37.90 eV and 35.75 eV, corresponding to W $4f_{5/2}$ and W $4f_{7/2}$ states, respectively. Notably, both W $4f_{5/2}$ and W $4f_{7/2}$ in the Ti–$WO_3$ nanosheets exhibited a slightly negative shift, implying that some electrons were transferred to $W^{6+}$ after Ti doping, resulting in more $W^{5+}$ species.[35] This phenomenon was due to the partial replacement of $W^{6+}$ by the Ti atoms.[41] In addition, there was no Ti 2p signal detected in the $WO_3$ nanosheets, while Ti 2p in the Ti–$WO_3$ nanosheets showed two peaks at 458.7 eV and 464.4 eV, which could be ascribed to the Ti(IV) $2p_{3/2}$ peak and the Ti(IV) $2p_{1/2}$ peak (Fig. 1F). This result was in accordance with the conclusion drawn from synchrotron–radiation X-ray absorption near-edge spectroscopy (XANES), which showed that the valence state of Ti in the Ti–$WO_3$ nanosheets was +4 (Fig. S2†). The content of Ti in the Ti–$WO_3$ nanosheets determined using inductively

coupled plasma atomic emission spectroscopy (ICP-OES) was 0.87 wt%, which was close to that determined by the XPS results (0.90 wt%). Furthermore, the annular dark-field TEM image and the corresponding element mappings revealed that there was no $TiO_2$ particle observed and the W, O and Ti elements were distributed uniformly (Fig. S3†). The Raman spectra also demonstrated that there was no additional peak detected in the Ti–$WO_3$ nanosheets (Fig. S4†), excluding the possibility of $TiO_2$/$WO_3$ heterojunction formation. Thus, these results showed that the Ti dopants had been doped in the $WO_3$ nanosheets and the valence state of Ti in the Ti–$WO_3$ nanosheets was +4.
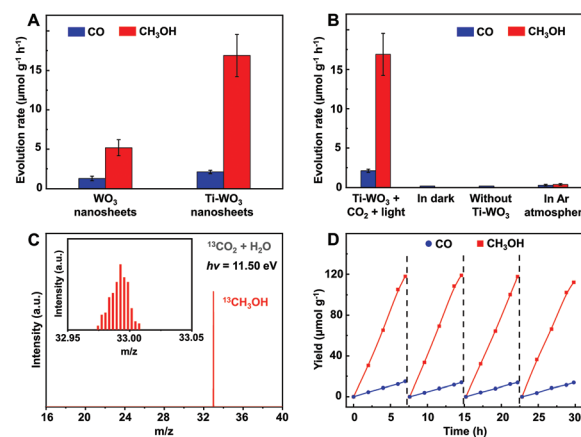
To investigate the effect of Ti dopants on the electronic band structures, ultraviolet–visible (UV–vis) absorption spectra were recorded. As shown in Fig. 2A, the absorption spectrum of the Ti–$WO_3$ nanosheets showed a red-shift compared with that of the $WO_3$ nanosheets, implying the stronger visible light absorption on the Ti–$WO_3$ nanosheets.[21,31,35] In addition, the bandgap of the Ti–$WO_3$ nanosheets determined using the absorption spectra was 2.59 eV (Fig. 2B), which was smaller than that of the $WO_3$ nanosheets (2.66 eV). To obtain the band edge potentials of the samples, synchrotron–radiation photoemission spectroscopy (SRPES) was applied to measure the work functions and the valence band maxima (VBM).[36] As shown in Fig. 2C and D, the work functions of the Ti–$WO_3$ nanosheets and the $WO_3$ nanosheets could be calculated to be 4.30 and 4.53 eV, whereas their valence-band edges were located at 2.27 eV and 2.48 eV. Combined with the bandgaps obtained above, the electronic band structures of the Ti–$WO_3$ nanosheets and the $WO_3$ nanosheets could be estimated (Table S1†). It was obvious that both samples had suitable electronic band structures for reducing $CO_2$ to $CH_3OH$, confirming their potential applications in $CO_2$ photoreduction.[5]

To evaluate the effect of Ti dopants on the catalytic activity, photocatalytic $CO_2$ reduction experiments were carried out. The liquid products were analyzed using nuclear magnetic resonance (NMR) spectroscopy, while the gas products were analyzed using a gas chromatograph (GC) equipped with a thermal conductivity detector (TCD) and a flame ionization detector (FID). As displayed in Fig. 3A, $CH_3OH$ was the major product of $CO_2$ photoreduction on both the samples, since the CO evolution rate was much lower than the $CH_3OH$ evolution rate. The $CH_3OH$ evolution rate on the Ti–$WO_3$ nanosheets could reach 16.8 μmol $g^{-1}$ $h^{-1}$, which was about 3.3 times higher than that on the $WO_3$ nanosheets, suggesting that Ti doping could efficiently promote the catalytic activity of $WO_3$ nanosheets. The selectivity towards $CH_3OH$ also increased from 80.0% to 88.9%. In addition, the $CH_3OH$ evolution rate was related to the amount of Ti dopants (Fig. S5†), indicating that Ti doping was a feasible strategy to adjust the performance of $WO_3$ nanosheets during the $CO_2$ photoreduction. What's more, the control experiments demonstrated that $CO_2$, the Ti–$WO_3$ nanosheets (catalyst) and illumination were prerequisites for the $CH_3OH$ formation, indicating that $CH_3OH$ was derived from photocatalytic $CO_2$ reduction over the Ti–$WO_3$ nanosheets (Fig. 3B). This conclusion could be further verified by the $^{13}CO_2$ labelling experiments performed with synchrotron-based vacuum ultraviolet photoionization mass spectrometry (SVUV-PIM). As shown in Fig. S6,† $N_2$, CO and $CO_2$ could not be ionized when the photon energy was set at 11.50 eV, and thus one could eliminate the interference from their fragments.[42] Hence, the Ti–$WO_3$ nanosheets produced the product $^{13}CH_3OH$ ($m/z$ = 33), confirming that evolved $CH_3OH$ indeed originated from the photoreduction of $CO_2$ (Fig. 3C). Furthermore, the $CH_3OH$ evolution rate showed almost no decay after 4 cycles of the photoreduction test (Fig. 3D), indicating the good photocatalytic stability of the



Fig. 2 (A) UV–vis absorption spectra and (B) the corresponding optical bandgaps for the Ti–$WO_3$ nanosheets and the $WO_3$ nanosheets. (C) Secondary electron cutoff and (D) valence band spectra of the Ti–$WO_3$ nanosheets and the $WO_3$ nanosheets acquired by synchrotron–radiation photoemission spectra.



Fig. 3 (A) Products of the photocatalytic $CO_2$ reduction over the Ti–$WO_3$ nanosheets and the $WO_3$ nanosheets. The error bars represent the standard deviations of three independent measurements. (B) Products of photocatalytic $CO_2$ reduction over the Ti–$WO_3$ nanosheets under different conditions. (C) SVUV-PIMS spectrum of the products during $^{13}CO_2$ labeled photoreduction over the Ti–$WO_3$ nanosheets at $h\nu$ = 11.50 eV. Inset: signals of $m/z$ = 33 ($^{13}CH_3OH$). (D) Cycling measurements for $CO_2$ photoreduction over the Ti–$WO_3$ nanosheets.

Ti–WO$_3$ nanosheets. The corresponding XRD patterns and TEM images after catalysis could also affirm the good stability of the Ti–WO$_3$ nanosheets (Fig. S7†).

To unravel the true active sites during CO$_2$ photoreduction over the Ti–WO$_3$ nanosheets, quasi *in situ* XPS spectra were used to investigate the change in electron density on the W sites. As shown in Fig. 4A and B, the content of W$^{5+}$ increased distinctly upon light irradiation of the reaction system, indicating that the W sites accepted the photoexcited electrons and generated W$^{5+}$ active species during the reaction. Once CO$_2$ was introduced into the system, the ratio of W$^{5+}$/W$^{6+}$ decreased from 0.38 to 0.25, indicating that the W$^{5+}$ ions were reoxidized into the original W$^{6+}$ ions by donating electrons to the adsorbed CO$_2$ molecules.[43] In addition, the valence state of the W atoms recovered to the initial state after removing the light irradiation (Fig. 3C) and the same trend was also detected on the WO$_3$ nanosheets (Fig. S8†). Notably, the W$^{5+}$ content in the Ti–WO$_3$ nanosheets was higher than that in the WO$_3$ nanosheets in the dark and it increased after the introduction of CO$_2$, implying that CO$_2$ was adsorbed on the W sites (Fig. 4D). On the contrary, the quasi *in situ* X-ray absorption near-edge spectroscopy (XANES) spectra revealed that the L-edge of Ti did not have any distinct changes during the whole process (Fig. S9†), indicating that the doped Ti atoms did not participate in the CO$_2$ photoreduction directly. This further certified that the true active sites over the Ti–WO$_3$ nanosheets were the W sites rather the Ti sites. Interestingly, the ratio of W$^{5+}$/W$^{6+}$ on the Ti–WO$_3$ nanosheets was lower than that on the WO$_3$ nanosheets under light irradiation, suggesting that more photoexcited electrons were donated to the adsorbed CO$_2$ molecules for photoreduction. In other words, the Ti dopants could facilitate the charge transfer on the Ti–WO$_3$ nanosheets to enhance the CO$_2$RR performance, where the separation of photogenerated carriers on the Ti–
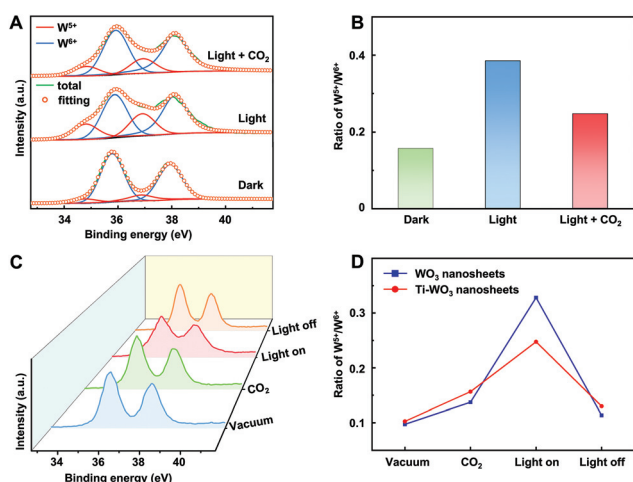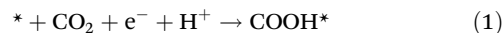


Fig. 4 (A) Quasi *in situ* XPS spectra and (B) the corresponding W$^{5+}$/W$^{6+}$ ratio of the Ti–WO$_3$ nanosheets under different atmospheres. (C) Quasi *in situ* XPS spectra of the Ti–WO$_3$ nanosheets during the CO$_2$ photoreduction. (D) The comparison of the W$^{5+}$/W$^{6+}$ ratio of the Ti–WO$_3$ nanosheets and the WO$_3$ nanosheets during the CO$_2$ photoreduction.
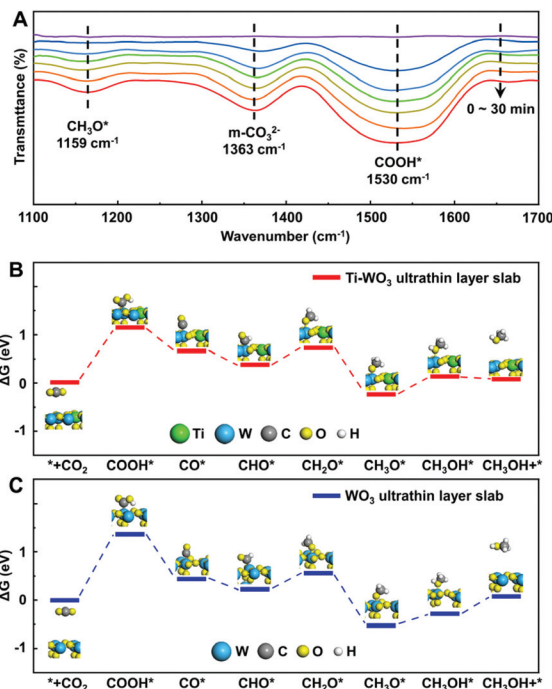


Fig. 5 (A) *In situ* FTIR spectra of the Ti–WO$_3$ nanosheets. (B) Free energy diagrams of CO$_2$ photoreduction to CH$_3$OH over the Ti–WO$_3$ ultrathin layer slab. (C) Free energy diagrams of CO$_2$ photoreduction to CH$_3$OH over the WO$_3$ ultrathin layer slab.

WO$_3$ nanosheets was also promoted, as revealed by the impedance test, transient photocurrent response, photo-luminescence (PL) and time-resolved photoluminescence (TRPL) spectra (Fig. S10 and S11†).[17,31]

To find out the reaction intermediates of CH$_3$OH formation on the Ti–WO$_3$ nanosheets, *in situ* FTIR measurement was carried out. As shown in Fig. 5A, three peaks appeared at 1158 cm$^{-1}$, 1365 cm$^{-1}$ and 1530 cm$^{-1}$. Similar peaks also appeared in the *in situ* FTIR spectra of the pristine WO$_3$ nanosheets, indicating the same CO$_2$ reduction process (Fig. S12†). The peak at 1530 cm$^{-1}$ could be assigned to COOH*, which was one of the most important intermediates for carbon products during CO$_2$ reduction.[36,42,44] Meanwhile, it was found that the peak density of COOH* on the Ti–WO$_3$ nanosheets was higher than that on the WO$_3$ nanosheets (Fig. S12†), implying that the Ti dopants might benefit CH$_3$OH formation through promoting the generation of COOH* intermediates. The peak at 1365 cm$^{-1}$ was assigned to m-CO$_3^{2-}$, which could be due to the dissolved CO$_2$ in the water.[45] In addition, the peak at 1158 cm$^{-1}$ could be ascribed to CH$_3$O*, which was one of the intermediates for CH$_3$OH formation.[42,44] Based on the results of *in situ* FTIR spectra, the possible reaction pathways could be summarized as follows:

$$* + CO_2 + e^- + H^+ \rightarrow COOH^* \quad (1)$$

$$COOH^* + e^- + H^+ \rightarrow CO^* + H_2O \quad (2)$$

$$CO^* + e^- + H^+ \rightarrow CHO^* \quad (3)$$

$$CHO^* + e^- + H^+ \rightarrow CH_2O^* \qquad (4)$$

$$CH_2O^* + e^- + H^+ \rightarrow CH_3O^* \qquad (5)$$

$$CH_3O^* + e^- + H^+ \rightarrow CH_3OH + ^* \qquad (6)$$

where the asterisks denote catalytically active sites in the reaction.

To further reveal the reason for the promotion of $CH_3OH$ formation on the Ti–$WO_3$ nanosheets, the Gibbs free energy of these key reaction pathways was calculated using DFT calculation (Fig. 5B and C and Table S4†). The calculation results suggested that the rate-limiting step was the formation of $COOH^*$ intermediates for both the samples,[46,47] while the reaction energy from $CO_2$ to $COOH^*$ was decreased from 1.37 to 1.15 eV over the Ti–$WO_3$ ultrathin layer slab, indicating a lower activation barrier of $CO_2$ on the $WO_3$ nanosheets after Ti doping. This could be attributed to the strengthened bonding between $COOH^*$ intermediates and the catalyst (Fig. S13†),[44] which could stabilize and generate more $COOH^*$ intermediates during the $CO_2$ photoreduction, well consistent with the *in situ* FTIR results. Furthermore, the energy barrier of $CH_3OH$ desorption over the Ti–$WO_3$ ultrathin layer slab was −0.06 eV, obviously lower than that of 0.36 eV over the $WO_3$ ultrathin layer slab, implying that the Ti dopants could also facilitate the $CH_3OH$ desorption, which was an important process for $CH_3OH$ formation. Thus, it was rational to conclude that doping Ti into $WO_3$ nanosheets could lower the reaction energy barrier, stabilize the $COOH^*$ intermediates and make $CH_3OH$ easier to desorb, thus improving the $CH_3OH$ yield during the $CO_2$ photoreduction.

## Conclusions

In summary, the ultrathin Ti-doped $WO_3$ nanosheets were successfully fabricated as an efficient catalyst for selectively photoreducing $CO_2$ and $H_2O$ into $CH_3OH$. XPS, XANES and element mappings showed the successful doping of Ti into the $WO_3$ nanosheets, while the PL and TRPL spectra demonstrated that the separation of photogenerated carriers on the Ti-doped $WO_3$ nanosheets were significantly promoted. Quasi *in situ* XPS spectra and quasi *in situ* XANES spectra firmly confirmed that the true active sites were the W sites rather the Ti sites, where the Ti dopants could facilitate the charge transfer, which was beneficial for the formation of $COOH^*$ species. *In situ* FTIR spectroscopy demonstrated this conclusion through the stronger intensity of $COOH^*$ species on the Ti-doped $WO_3$ nanosheets, while DFT calculations showed that Ti doping could strengthen the bonding between $COOH^*$ intermediates and the catalyst. In addition, the Gibbs free energy calculations also indicated that the activation barrier of $CO_2$ was decreased from 1.37 to 1.15 eV, while the energy barrier of $CH_3OH$ desorption was decreased from 0.36 to −0.06 eV on the Ti–$WO_3$ nanosheets, thus promoting the formation of $CH_3OH$. In consequence, the Ti-doped $WO_3$ ultrathin nanosheets exhibited a superior $CH_3OH$ selectivity of 88.9%

and achieved a methanol evolution rate of 16.8 μmol g$^{-1}$ h$^{-1}$, about 3.3 times higher than that on the $WO_3$ nanosheets. This work offers an effective approach to photoreduce $CO_2$ into $CH_3OH$ and renders a deep insight to promote the performance of catalysts during the photoreduction reaction.

## Author contributions

Y. Xie, Y. F. Sun, P. Q. Ling and J. C. Zhu conceived the idea and co-wrote the paper. P. Q. Ling and Z. Q. Wang carried out the sample synthesis, characterization and $CO_2$ photoreduction measurement. J. C. Zhu conducted DFT calculations. J. Hu and J. F. Zhu conducted the quasi *in situ* XPS and quasi *in situ* XANES measurement. W. S. Yan conducted the synchrotron–radiation XANES measurement. All the authors contributed to the overall scientific interpretation and edited the manuscript.

## Conflicts of interest

There are no conflicts to declare.

## Acknowledgements

## References

1 N. Kornienko, J. Z. Zhang, K. K. Sakimoto, P. Yang and E. Reisner, *Nat. Nanotechnol.*, 2018, **13**, 890–899.
2 X. B. Li, Z. K. Xin, S. G. Xia, X. Y. Gao, C. H. Tung and L. Z. Wu, *Chem. Soc. Rev.*, 2020, **49**, 9028–9056.
3 X. Li, J. Yu, M. Jaroniec and X. Chen, *Chem. Rev.*, 2019, **119**, 3962–4179.
4 X. Chang, T. Wang, P. Yang, G. Zhang and J. Gong, *Adv. Mater.*, 2019, **31**, 1804710.
5 S. Navarro-Jaén, M. Virginie, J. Bonin, M. Robert, R. Wojcieszak and A. Y. Khodakov, *Nat. Rev. Chem.*, 2021, **5**, 564–579.
6 H. Zhao, J. Duan, Z. Zhang and W. Wang, *ChemCatChem*, 2021, **14**, 202101733.

7 X. Chang, T. Wang, Z. J. Zhao, P. Yang, J. Greeley, R. Mu, G. Zhang, Z. Gong, Z. Luo, J. Chen, Y. Cui, G. A. Ozin and J. Gong, *Angew. Chem., Int. Ed.*, 2018, **57**, 15415–15419.

8 Z. H. Li, H. Zeng, G. Zeng, C. Ru, G. Li, W. Yan, Z. Shi and S. Feng, *Angew. Chem., Int. Ed.*, 2021, **60**, 26577–26581.

9 A. Goeppert, M. Czaun, J. P. Jones, G. K. Surya Prakash and G. A. Olah, *Chem. Soc. Rev.*, 2014, **43**, 7995–8048.

10 C. H. Vo, C. Mondelli, H. Hamedi, J. Pérez-Ramírez, S. Farooq and I. A. Karimi, *ACS Sustainable Chem. Eng.*, 2021, **9**, 10591–10600.

11 B. Han, X. Ou, Z. Deng, Y. Song, C. Tian, H. Deng, Y. J. Xu and Z. Lin, *Angew. Chem., Int. Ed.*, 2018, **57**, 16811–16815.

12 H. L. Nguyen and A. Alzamly, *ACS Catal.*, 2021, **11**, 9809–9824.

13 W. Guo, S. Liu, X. Tan, R. Wu, X. Yan, C. Chen, Q. Zhu, L. Zheng, J. Ma, J. Zhang, Y. Huang, X. Sun and B. Han, *Angew. Chem., Int. Ed.*, 2021, **60**, 21979–21987.

14 Y. Wang, X. Liu, X. Han, R. Godin, J. Chen, W. Zhou, C. Jiang, J. F. Thompson, K. B. Mustafa, S. A. Shevlin, J. R. Durrant, Z. Guo and J. Tang, *Nat. Commun.*, 2020, **11**, 2531.

15 S. C. Shit, I. Shown, R. Paul, K. H. Chen, J. Mondal and L. C. Chen, *Nanoscale*, 2020, **12**, 23301–23332.

16 M. Wang, M. Shen, X. Jin, J. Tian, M. Li, Y. Zhou, L. Zhang, Y. Li and J. Shi, *ACS Catal.*, 2019, **9**, 4573–4581.

17 Y. He, H. Rao, K. Song, J. Li, Y. Yu, Y. Lou, C. Li, Y. Han, Z. Shi and S. Feng, *Adv. Funct. Mater.*, 2019, **29**, 1905153.

18 M. Zhou, S. Wang, P. Yang, C. Huang and X. Wang, *ACS Catal.*, 2018, **8**, 4928–4936.

19 Y. Bo, C. Gao and Y. Xiong, *Nanoscale*, 2020, **12**, 12196–12209.

20 T. Kong, Y. Jiang and Y. Xiong, *Chem. Soc. Rev.*, 2020, **49**, 6579–6591.

21 Y. Mi, L. Wen, Z. Wang, D. Cao, R. Xu, Y. Fang, Y. Zhou and Y. Lei, *Nano Energy*, 2016, **30**, 109–117.

22 J. He, C. Wu, Y. Li and C. Li, *J. Mater. Chem. A*, 2021, **9**, 19508–19533.

23 F. Zhang, J. Zhang, B. Zhang, L. Zheng, X. Cheng, Q. Wan, B. Han and J. Zhang, *Nat. Commun.*, 2020, **11**, 1431.

24 Y. Zhao, Y. Zhao, G. I. N. Waterhouse, L. Zheng, X. Cao, F. Teng, L. Z. Wu, C. H. Tung, D. O'Hare and T. Zhang, *Adv. Mater.*, 2017, **29**, 1703828.

25 S. Qamar, F. Lei, L. Liang, S. Gao, K. Liu, Y. Sun, W. Ni and Y. Xie, *Nano Energy*, 2016, **26**, 692–698.

26 X. Li, L. Liang, Y. Sun, J. Xu, X. Jiao, X. Xu, H. Ju, Y. Pan, J. Zhu and Y. Xie, *J. Am. Chem. Soc.*, 2019, **141**, 423–430.

27 J. Fu, K. Liu, K. Jiang, H. Li, P. An, W. Li, N. Zhang, H. Li, X. Xu, H. Zhou, D. Tang, X. Wang, X. Qiu and M. Liu, *Adv. Sci.*, 2019, **6**, 1900796.

28 X. Li, S. Wang, L. Li, X. Zu, Y. Sun and Y. Xie, *Acc. Chem. Res.*, 2020, **53**, 2964–2974.

29 Y. Xu, J. Mo, G. Xie, X. Wang and S. Ding, *J. Mater. Chem. A*, 2020, **8**, 4457–4463.

30 T. Chen, T. Liu, X. Shen, W. Zhang, T. Ding, L. Wang, X. Liu, L. Cao, W. Zhu, Y. Li and T. Yao, *Sci. China Mater.*, 2021, **64**, 2997–3006.

31 L. K. Putri, B.-J. Ng, W.-J. Ong, H. W. Lee, W. S. Chang and S.-P. Chai, *J. Mater. Chem. A*, 2018, **6**, 3181–3194.

32 Y. Ding and P. Nagpal, *Nanoscale*, 2016, **8**, 17496–17505.

33 C. Mao, F. Zuo, Y. Hou, X. Bu and P. Feng, *Angew. Chem., Int. Ed.*, 2014, **53**, 10485–10489.

34 V. Kumaravel, J. Bartlett and S. C. Pillai, *ACS Energy Lett.*, 2020, **5**, 486–519.

35 S. Sun, M. Watanabe, J. Wu, Q. An and T. Ishihara, *J. Am. Chem. Soc.*, 2018, **140**, 6474–6482.

36 L. Liang, X. Li, Y. Sun, Y. Tan, X. Jiao, H. Ju, Z. Qi, J. Zhu and Y. Xie, *Joule*, 2018, **2**, 1004–1016.

37 J. Ma, K. Mao, J. Low, Z. Wang, D. Xi, W. Zhang, H. Ju, Z. Qi, R. Long, X. Wu, L. Song and Y. Xiong, *Angew. Chem., Int. Ed.*, 2021, **60**, 9357–9361.

38 B. M. Klepser and B. M. Bartlett, *J. Am. Chem. Soc.*, 2014, **136**, 1694–1697.

39 G. Cai, X. Wang, D. Zhou, J. Zhang, Q. Xiong, C. Gu and J. Tu, *RSC Adv.*, 2013, **3**, 6896–6905.

40 S. S. Kalanur, I.-H. Yoo and H. Seo, *Electrochim. Acta*, 2017, **254**, 348–357.

41 Y. Zhan, M. R. J. Tan, X. Cheng, W. M. A. Tan, G. F. Cai, J. W. Chen, V. Kumar, S. Magdassi and P. S. Lee, *J. Mater. Chem. C*, 2017, **5**, 9995–10000.

42 W. Shao, S. Wang, J. Zhu, X. Li, X. Jiao, Y. Pan, Y. Sun and Y. Xie, *Nano Res.*, 2021, **14**, 4520–4527.

43 S. Zhu, X. Li, X. Jiao, W. Shao, L. Li, X. Zu, J. Hu, J. Zhu, W. Yan, C. Wang, Y. Sun and Y. Xie, *Nano Lett.*, 2021, **21**, 2324–2331.

44 X. Li, Y. Sun, J. Xu, Y. Shao, J. Wu, X. Xu, Y. Pan, H. Ju, J. Zhu and Y. Xie, *Nat. Energy*, 2019, **4**, 690–699.

45 Y. Wang, J. Zhao, T. Wang, Y. Li, X. Li, J. Yin and C. Wang, *J. Catal.*, 2016, **337**, 293–302.

46 Y. Li, S. Wang, X. S. Wang, Y. He, Q. Wang, Y. Li, M. Li, G. Yang, J. Yi, H. Lin, D. Huang, L. Li, H. Chen and J. Ye, *J. Am. Chem. Soc.*, 2020, **142**, 19259–19267.

47 P. Yang, H. Zhuzhang, R. Wang, W. Lin and X. Wang, *Angew. Chem., Int. Ed.*, 2019, **58**, 1134–1137.